

Contents lists available at [SciVerse ScienceDirect](http://www.sciencedirect.com)

Deep-Sea Research II

journal homepage: www.elsevier.com/locate/dsr2

Satellite views of Pacific chlorophyll variability: Comparisons to physical variability, local versus nonlocal influences and links to climate indices

Andrew C. Thomas^{a,*}, P. Ted Strub^b, Ryan A. Weatherbee^a, Corinne James^b

^a School of Marine Sciences, 5706 Aubert Hall, University of Maine, Orono, ME 04469, USA

^b College of Earth, Ocean and Atmospheric Sciences, Oregon State University, Corvallis, OR, USA

ARTICLE INFO

Keywords:

Pacific
Chlorophyll
Sea level
Surface temperature
Eastern boundary currents
Climate indices
Satellite data

ABSTRACT

Concurrent satellite-measured chlorophyll (CHL), sea surface temperature (SST), sea level anomaly (SLA) and model-derived wind vectors from the 13+ year SeaWiFS period September 1997–December 2010 quantify time and space patterns of phytoplankton variability and its links to physical forcing in the Pacific Ocean. The CHL fields are a metric of biological variability, SST represents vertical mixing and motion, often an indicator of nutrient availability in the upper ocean, SLA is a proxy for pycnocline depths and surface currents while vector winds represent surface forcing by the atmosphere and vertical motions driven by Ekman pumping. Dominant modes of variability are determined using empirical orthogonal functions (EOFs) applied to a nested set of domains for comparison: over the whole basin, over the equatorial corridor, over individual hemispheres at extra-tropical latitudes ($> 20^\circ$) and over eastern boundary current (EBC) upwelling regions. Strong symmetry exists between hemispheres and the EBC regions, both in seasonal and non-seasonal variability. Seasonal variability is strongest at mid latitudes but non-seasonal variability, our primary focus, is strongest along the equatorial corridor. Non-seasonal basin-scale variability is highly correlated with equatorial signals and the strongest signal across all regions in the study period is associated with the 1997–1999 ENSO cycle. Results quantify the magnitude and geographic pattern with which dominant basin-scale signals are expressed in extra-tropical regions and the EBC upwelling areas, stronger in the Humboldt Current than in the California Current. In both EBC regions, wind forcing has weaker connections to non-seasonal CHL variability than SST and SLA, especially at mid and lower latitudes. Satellite-derived dominant physical and biological patterns over the basin and each sub-region are compared to indices that track aspects of climate variability in the Pacific (the MEI, PDO and NPGO). We map and compare the local CHL footprint associated with each index and those of local wind stress curl, showing the dominance in most areas of the MEI and its similarity to the PDO. Principal estimator patterns quantify the linkage between dominant modes of forcing variability (wind, SLA and SST) and CHL response, comparing local interactions within EBC regions with those imposed by equatorial signals and mapping equatorial forcing on extra-tropical CHL variability.

© 2012 Elsevier Ltd. All rights reserved.

1. Introduction

The climatological pattern of surface phytoplankton biomass over the Pacific basin (Fig. 1) reflects dominant patterns of heating, wind stress and stratification that control the flux of subsurface nutrients into the euphotic zone. Seasonal variability about this pattern is dominated by mid-latitude shifts in the location of the transition zone separating oligotrophic subtropical gyre waters from more productive waters at higher latitudes (Longhurst, 1995; Vantrepotte and Mélin, 2009; Yoder and Kennelly, 2003). Elsewhere, responses to interannual forcing, often of equatorial origin such as

the El Niño Southern Oscillation (ENSO), can be of similar magnitude or larger than local seasonal cycles (e.g., Chavez et al., 1999; Martinez et al., 2009; Vantrepotte and Mélin, 2011; Yoder and Kennelly, 2003), transmitted through atmospheric teleconnections (e.g., Chhak and DiLorenzo, 2007; Schwing et al., 2010) and oceanic pathways (e.g., Hormazabal et al., 2001; Strub and James, 2002c). Along the eastern basin margins, the biologically productive California and Humboldt eastern boundary current (EBC) upwelling systems respond rapidly and strongly to basin scale signals imposed from lower latitudes (Carr et al., 2002; Kahru and Mitchell, 2000) as well as higher latitudes (Freeland et al., 2003; Wheeler et al., 2003). Such EBC variability is superimposed on more locally controlled variability driven by latitudinally modulated seasonal wind forcing and heating (Bakun and Nelson, 1991; Thomas et al., 2001b). The energetic structure and relatively strong time and space gradients of

* Corresponding author. Tel.: +1 207 581 4335; fax: +1 207 581 4388.
E-mail address: thomas@maine.edu (A.C. Thomas).

biomass. Temporally coincident missions measured physical processes that potentially modulate phytoplankton patterns: SST (a metric of surface stratification, mixing and nutrient availability) and SLA (a metric of pycnocline depth and current structure). We augment these with model wind stress (wind stress curl: the driver of Ekman pumping/suction and alongshore wind stress: the driver of coastal upwelling). Against a background of better known seasonal CHL variability (Vantrepotte and Mélin, 2009; Yoder et al., 2010), our objectives are to relate satellite-derived fields of CHL to fields of SLA, SST and wind stress in the Pacific Basin in order to: (1) contrast the synoptic modes of variability of CHL with physical variables, including the degree of symmetry between hemispheres; (2) relate basin-scale signals to those of the two Pacific EBC regions, comparing them to local forcing; and (3) relate satellite-derived statistical modes to three indexes of climate variability, the MEI, PDO and the NPGO. For completeness, we recognize our study areas have links to variability in the western Pacific basin (Miller et al., 2004) that are not addressed here.

2. Data and methods

SeaWiFS monthly-averaged CHL over the duration of the mission (September 1997–December 2010) were obtained from the NASA ocean color server. CHL values are the standard NASA chlorophyll algorithm (O'Reilly et al., 1998), reprocessing version R2010. Instrument difficulties create four data gaps of 2–4 months duration in 2008 and 2009. At latitudes $> \sim 50^\circ$, few data are available during hemisphere winter months due to darkness. We work with log transformed CHL values, consistent with previous work showing their underlying distribution (Campbell, 1995). Even in the monthly means, CHL retrievals at some pixels in this data set have some suspiciously high values, likely a result of localized failures in atmospheric correction, cloud edge effects and/or bio-optical algorithm failure in turbid water, creating noisy fields. We reduce this noise in a series of steps, cognizant of our focus on longer time/space scale signals. Values greater than 30 mg m^{-3} were flagged as missing. Data were then \log_{10} transformed and at each location values greater than the climatological mean plus two standard deviations were also flagged as missing. Data were transformed back into chlorophyll space and a 3×3 median spatial operator was then passed over each monthly field twice, and then transformed back into \log_{10} units and the climatological mean at each location was removed. We use two time series, (log transformed) CHL concentrations with zero mean at each location (retaining seasonality) and monthly anomalies created by subtracting the climatological months from each year at each location.

Maps of 1/4 degree SLA gridded from multiple satellites were obtained from AVISO (<http://www.aviso.oceanobs.com>). For September 1997–November 2010, monthly averages were created from available weekly fields of the AVISO Updated Delayed Time sea level anomaly product. We extended the SLA time series one month through December 2010 using “near real time” SLA data for consistency with the other time series. For June 2010 through December 2010, daily fields of the AVISO Daily Merged Near Real Time SLA data were averaged into monthly means. The two monthly time series were combined into a single monthly time series spanning September 1997–December 2010 using a weighted average to smooth the transition between the Delayed Time and the Near Real Time data. EOFs calculated with and without the last added month (merged data) were indistinguishable, beyond extending the time series to match the CHL data. The time average for each point was removed. Subtracting the climatological months from this time series created anomaly fields.

Monthly average fields of optimally interpolated Reynolds SST version 2, Ol.v2 (Reynolds et al., 2002), on a 1° grid were obtained from the Environmental Modeling Center at the National Weather Service (ftp://ftp.emc.ncep.noaa.gov/cmb/sst/oimonth_v2/). The time average was removed from each spatial data point. Climatological months were computed for the period September 1997–December 2010 and subtracted from the time series to create anomalies.

ECMWF ERA-Interim Project wind data are used. These six-hourly horizontal wind fields from NCAR's Data Support Section are used to calculate wind stress and wind stress curl using a variable drag coefficient (Large et al., 1995), then averaged into monthly values. The time average for each point was removed. Subtracting the climatological monthly means from these created anomaly fields. The time series at each location was smoothed using a 3-month boxcar filter. The monthly means remove variability on the scale of synoptic storms and upwelling events of several days. As we are primarily interested in quantifying the large-scale, interannual differences in vertical motion of nutrients beneath the mixed layer driven by Ekman transports (coastal upwelling and open-ocean Ekman pumping), alternating fluctuations on shorter time scales will average into the monthly means in a linear fashion. Primary production, however, is not reversible and so is not a linear process. An analysis of event-scale responses of phytoplankton to wind forcing is beyond the scope of our large-scale analysis, but must be kept in mind while interpreting our results. Such a study would require different statistical techniques and is worthy of a separate investigation.

Data over marginal seas of the Pacific (e.g., the Bering, Okhotsk, Japan, South China, Gulf of California) are excluded from each spatial field to focus analysis on the Pacific basins and their EBCs (Fig. 1). The final data set is a concurrent, 160-month time series of CHL, SST, SLA and wind stress anomalies.

Empirical orthogonal functions (EOFs) isolate dominant modes of satellite-measured variability over a series of nested study domains. EOFs are empirical in the sense that the space/time patterns are purely a function of the variance present in the target data set making them sensitive to the space and time domain of the data set. We exploit this characteristic to compare dominant modes calculated over the whole Pacific basin with those over just the equatorial region ($0^\circ \pm 20^\circ$), within each higher-latitude hemisphere (20° – 60°) and then within each EBC upwelling region (Fig. 1). Due to strong, often non-coherent variability in both time and space in these data, even the dominant modes often capture relatively small percentages of the total variance over such large regions. These, however, are the dominant coherent time/space patterns in the data that are the focus of our investigation.

Significance of the resulting EOF modes can be discussed from three perspectives; statistical significance of the modes, relative separation of the eigenvalues of each mode, and the bio-physical realism of the time/space pattern. First, to examine statistical significance we use the *N*-rule approach outlined by Overland and Preisendorfer (1982) to estimate those eigenvalues for which the geophysical signal exceeds the level of noise within the data. For all the EOFs calculated here, each of the first three modes (we present, at most, the dominant 2) exceeds the noise level by this criterion. Second, limitations in sampling of the signals in question can mean that eigenvalues that are very similar may not provide realistic separation of underlying actual patterns in the data set (Deser et al., 2010; Dommenges and Latif, 2002; North et al., 1982). We examined each of the first three modes of the EOFs we present for separation using the rule of thumb suggested by North et al. (1982). Of the 24 modes presented, the eigenvalues of all but 3 are statistically separate from that of the following mode. The three questionable modes are each over the South Pacific and we discuss our interpretation of them when they are presented. Lastly, caution should be exercised in interpretation of

Messié and Radenac, 2006; Thomas et al., 2001b; Vantrepotte and Mélin, 2009; Yoder and Kennelly, 2003) but included here to provide the background against which non-seasonal patterns can be compared. They also highlight the seasonal symmetry between the two hemispheres and their respective EBC regions and document the complete SeaWiFS mission not included in previous studies. Over the entire basin and in the California and Humboldt EBC regions, the first two modes capture most of the seasonal structure (47%, 41%, and 32% of total variance, respectively) with relatively weak interannual differences over their 13+ year time series. The third modes (not shown) have strong non-seasonal signals, analyzed separately in the following sections. Time and space patterns in the first two modes of the entire basin calculated over the 13+ years are generally similar to those evident over the Pacific in a global EOF analysis of a 4-year period (1998–2001) presented by Yoder and Kennelly (2003), indicative of both the temporal and spatial stability of the overall seasonal structure.

Over the whole basin (Fig. 2(A)), mode 1 is dominated by mid latitude annual cycles, maximum in hemisphere winter, representing seasonal shifts in the location of the frontal transition zone separating oligotrophic subtropical gyre waters from more productive waters at higher latitudes (Fig. 1). Highest latitudes in both hemispheres (> about 45°) have the opposite sign, creating summer maxima. Together, these capture the transition from a nutrient limited to a light limited annual cycle (Dandonneau et al., 2004). Patterns at low latitudes (< 20°) are relatively weak except along the far eastern margin in the vicinity of wind-jets at Central America's mountain gaps (Chelton et al., 2000) and in the Peru upwelling region, consistent with previously shown EBC seasonality (Echevin et al., 2008; Thomas et al., 2009). Mode 2 is 3 months out of phase with mode 1 (maxima in May and November), allowing the combination of the two modes to describe a smooth meridional shift of the mid-latitude extrema. This mode also includes maxima with different signs at the Central American mountain gaps, in the Southern Ocean and in the EBC upwelling regions off North America and Chile. The most prominent features are a basin-wide zonal positive band at ~10°N paired with a weaker, less extensive, negative zonal maximum at ~10°S describing CHL maxima in early summer of each hemisphere. Spatially, these track climatological patterns of wind stress curl associated with positive vertical velocity (Risien and Chelton, 2008; Talley et al., 2011).

In EBC regions (Fig. 2(B)), mode 1 maxima are present along each coastal upwelling region, maximum in each hemisphere's summer, accompanied by weaker offshore maxima in the hemisphere's winter. These are ~1 month earlier in the California Current than those over the whole basin and the Humboldt Current, consistent with analyses of shorter records (Thomas et al., 2001b). Elevated coastal concentrations are strongest/widest in the Pacific Northwest and off Baja California in the California Current and off central Peru and central-southern Chile in the Humboldt Current, weakest and narrow off northern Chile and reversed along southern California. Mode 2 captures additional seasonality, primarily in the upwelling regions of the southern California Current and Peru. Opposite-phased maxima occur at higher latitudes, especially central Chile. The April (positive) maximum in the time series in both EBCs initiates elevated concentrations early in the summer season off Baja and southern California (Espinosa-Carreón et al., 2004) and extends the summer high values later in the season off Peru. The September and November negative maxima describe weak late summer high latitude peaks in the California Current and stronger spring peaks off Chile, respectively.

3.2. Basin-scale non-seasonal variability

Removing the climatological monthly fields from each time series produces the non-seasonal signals highlighting interannual

variability, the primary focus of this study. In contrast to seasonal signals, the two dominant modes of non-seasonal CHL variability (23% of total non-seasonal variance) over the basin (Fig. 3(A)) are centered on the equatorial region. The first mode CHL spatial pattern is highlighted by a strong westward pointing "arrowhead" shaped positive feature, centered at the equator, maximum ~160°E to 160°W. Three fingers of elevated variability extend eastward from this maximum, one north of the equator at ~10°N extending east and continuous with elevated variability off Central America, one at the equator that extends east to ~140°W and the third tracking southeast into the South Pacific to ~20°S at 120°W. These resemble features isolated as both multi-year trend and non-stationary seasonality by Vantrepotte and Mélin (2011). Their relation to seasonality is evident here as the northern and southern "fingers" overlay almost exactly the positive/negative zonal bands of the mode 2 seasonal CHL pattern (Fig. 2(A)). Smaller positive areas are along the coast of Peru, Mexico and off southern California, with weak positive regions at higher (> 40°) latitudes. The strongest negative pattern is in the far western equatorial Pacific north of New Guinea. The time series is dominated by strong negative values during the 1997–1998 El Niño (Chavez et al., 1999; McPhaden, 1999; Strub and James, 2002a). Thereafter, three periods are evident, generally positive in 1999–2001, negative in 2002–2007 and positive again in 2007–2009. In mode 2, the strongest features reflect additional variability associated with the same features as mode 1: negative values in the western warm pool are centered at ~160°E extending northeast along the mode 1 northern finger, a relative minimum also extends along the southern edge of the southern mode 1 finger. Strong positive patterns are associated with features off Central America, in phase with features in the EBC upwelling regions, strongest close to the coast. The mode 2 time series is strongly negative in 1997 and early 1998, weakens relatively slowly and becomes positive in 2001, remaining so until 2008. Together, these two modes describe a large region of negative CHL anomalies across the equatorial Pacific during the 1997–1998 El Niño period with positive CHL anomalies in the west. The positive anomalies spread eastward as the time series become positive first for mode 1, followed by mode 2. During 2008–2010, mode 1 reflects conditions that switched from La Niña to El Niño and back.

SLA variability (Fig. 3(B)), a tracer of changes in upper mixed layer thickness and nutricline depth (Polovina et al., 1995; Wilson and Adamec, 2001), is also predominantly focused on equatorial regions. In mode 1, a tongue of positive values extends from ~170°E eastward across the basin at the equator, continuous with a broad region along the eastern low latitude margins. West of 170°E, equatorial patterns are strongly negative from ~20°N to 10°S, with weaker negative regions extending into subtropical central basins at mid latitudes. The time series for this mode is dominated by strong positive values in 1997–1998 during the El Niño. It switches to negative values from mid 1998 until 2002, with positive events in 2002–2003 and 2009–2010 associated with weaker El Niño events and obviously mirrors the CHL signal. SLA mode 2 isolates additional variability dominated by low latitude processes, strongly negative at low latitudes from the western side of the basin to ~110°W, with a weaker negative centered at ~45°N in the NE Pacific. This time series mirrors the CHL mode 2 signal, positive in mid 1998 during later stages of the ENSO cycle. Thereafter, its amplitude is weaker and mainly negative from 2001 to early 2010.

Basin-wide EOF modes of non-seasonal SST (not shown) are substantially similar to SLA, dominated by equatorial signals with maximum amplitudes during the 1997–1998 El Niño, patterns shown and discussed in previous work (Deser et al., 2010; Messié and Chavez, 2011). SLA and SST EOF time series are highly correlated across the first two modes (Table 1). EOFs of basin-scale

non-seasonal wind stress curl (not shown), however, are dominated by patterns over the Southern Ocean and neither their space nor time patterns resemble those of CHL, SST or SLA.

Comparisons between the CHL patterns and those of SLA (and SST) in mode 1 (Fig. 3) show the canonical association of lower (higher) CHL values with elevated (decreased) SLA, indicative of a thicker (thinner) mixed layer over the eastern basins and main basin gyres where signals are weaker (Wilson and Adamec, 2002). In equatorial regions where the signals are strong, CHL maxima appear most closely associated with the edges of SLA features, suggesting links to changes in the equatorial current structure (Wilson and Adamec, 2001). Space patterns in the two second modes are less similar and appear to capture different phases of transition in the ENSO cycle (McPhaden, 1999), an observation supported by slight differences in the timing of the 1998 maxima. The strong link between non-seasonal temporal CHL variability and satellite-measured physical variability evident in Fig. 3 is quantified in the correlations between modes 1 and 2 across CHL, SLA and SST (Table 1).

The extent of dominance of basin-scale non-seasonal modes by equatorial variability is investigated by calculating separate EOFs over a spatial domain restricted to $\pm 20^\circ$ of the equator (see Fig. 1). EOFs for CHL, SST and SLA in this equatorial corridor (not shown) have patterns that are essentially identical to those for the whole basin in the equatorial region of spatial overlap. Equatorial EOF time series are strongly correlated (all > 0.94) with those of their basin-scale counterpart (Table 1) in both modes 1 and 2.

3.3. Extra-tropical patterns, symmetry and relationships to basin-scale signals

Removing the equatorial signal isolates variability occurring at higher latitudes allowing comparisons of the degree to which hemispheres vary symmetrically and the extent to which higher-latitude variability tracks that at the equator. The dominant modes of CHL, SLA and SST EOFs calculated separately over $20\text{--}60^\circ$ latitude in each hemisphere (see Fig. 1) are presented in Fig. 4. In the northern hemisphere, mode 1 spatial patterns are generally similar among chlorophyll, SLA and SST, positive in eastern portions of the basin and negative over the central basin, strongest between 160° and 180°W . Their respective time series are well correlated (Table 2). In the southern hemisphere, strongest CHL variability is centered between $80^\circ\text{--}100^\circ\text{W}$ and $130^\circ\text{--}160^\circ\text{W}$ at mid latitudes. Variability south of 40°S (over the Southern Ocean) is weak except for a small region west of New Zealand. Mode 1 spatial patterns of SLA and SST are similar, strongest and positive over the Southern Ocean ($100^\circ\text{--}160^\circ\text{W}$), and negative, although with differences in latitude, over the eastern subtropical gyre and around New Zealand. Their time series are correlated (Table 2). These modes, however, are not correlated with that of CHL. CHL mode 1 is better related to mode 2 of both SLA and SST (Table 2), whose variance is also centered at mid latitudes between 130° and 160°W .

For each of these southern hemisphere EOF decompositions (Fig. 4), very similar eigenvalues (% variance explained) over the dominant 2–3 modes call into question their separability (North et al., 1982). We evaluate their separation and validity using a number of approaches. CHL mode 1 (Fig. 4(A), 10% of total variance) is not statistically separate from mode 2 (not shown). Recalculation of this EOF following increased smoothing of the initial monthly CHL fields (not shown) produced very similar space patterns and highly correlated time series over the dominant three modes, each of which was separate by North et al., (1982) rule of thumb. We take this as evidence that CHL mode 1 (Fig. 4(A)) is likely separate, but with statistics hidden by the

relatively noisy biological signal. For both SLA and SST we have access to additional data with which to compare our modes. Computation of an SLA EOF over the southern hemisphere region for the full period of AVISO data availability (October 1992–December 2010, i.e., five additional years) produces dominant modes (not shown) strongly resembling those presented and time series that are highly correlated over the time period of overlap (0.95 and 0.98, respectively). Each of the first three modes in this longer time series decomposition is statistically separate (North et al., 1982), evidence that our presented modes are also separate. A similar approach with SST data made use of a higher time and space resolution data set ($1/4$ degree, daily) with which we calculated EOFs over the period January 1982–December 2010 (i.e., ~ 16 years of additional data). The first three modes of this decomposition are clearly separate by North et al.'s criteria. The first two modes have spatial patterns similar to those in Fig. 4(C) with correlated time series (0.76, 0.71, for modes 1 and 2, respectively). Patterns resemble those with strongest variance over the Pacific presented by Messié and Chavez (2011). We take these as evidence that the presented modes are separate.

How symmetric is non-seasonal variability in the two hemispheres? Spatially, taking into account the longitudinal difference in the eastern basin margin of each hemisphere, Fig. 4 shows symmetry between the northern and southern hemispheres in spatial pattern for SST, consistent with previous results (Shakun and Shaman, 2009) and also for SLA, less so for CHL. Positive regions in the eastern portions of the basins mirror each other, expanding westward at lower and higher latitudes. Negative regions trend from mid latitudes in the east towards lower latitudes in the west. Temporally (Table 2), while correlations between modes 1 of each hemisphere of each measurement are statistically significant, only that of SST (0.72) appears similar over the whole study period (Fig. 4(C), bottom). Obvious differences in timing of specific events in CHL and SLA (Fig. 4(A) and (B)) are evident reducing their inter-hemisphere correlations. Respective second modes are not well correlated.

To what degree does dominant variability at higher latitudes reflect those calculated over the whole basin? This is relevant because many climate indices (e.g., the NPGO, PDO and North Pacific Oscillation) are defined by variability confined to higher latitudes in the North Pacific and the basin signals are strongly correlated to equatorial signals (Table 1). In the northern hemisphere, mode 1 space patterns of CHL, SLA and SST (Fig. 4) have clear similarity to their counterparts in the whole basin EOFs (Fig. 3, SST not shown). Strong correlation of their respective time series (Table 2), indicate that dominant northern hemisphere non-equatorial patterns reflect those over the basin and in the equatorial corridor. Despite these correlations, an obvious difference between the time series in Fig. 3 and those of Fig. 4 is the reduced relative strength of the 1997–1998 El Niño signal. At higher latitudes, variability later in the time series is often of equal, or greater, magnitude. Correlations between southern hemisphere and whole basin CHL and SLA are significant but weak, however those of SST are relatively strong (Table 2).

3.4. Eastern boundary current variability

Satellite-measured non-seasonal CHL variability in the Pacific EBC upwelling regions is relatively well documented over specific times and regions (Carr et al., 2002; Kahru and Mitchell, 2001, 2002; Thomas et al., 2003). Here we focus on dominant coherent variability over the entire EBC domains, their relative symmetry in the two hemispheres and their similarity to concurrent physical signals. The first EOF modes of CHL variability (Fig. 5(A), 18% and 16% of the total variance in the California and Humboldt regions, respectively) show the strongest signals over the study period in

Table 2

Correlations between dominant EOF modes of North Pacific, South Pacific and whole-basin time series of non-seasonal chlorophyll, SLA and SST (Fig. 4).

Region	N. Pacific					S. Pacific					Whole basin		
	CHL M1	SLA M1	M2	SST M1	M2	CHL M1	SLA M1	M2	SST M1	M2	CHL M1	SLA M1	SST M1
N. Pacific													
CHL													
M1	1	−0.57	–	−0.71	–	0.40	–	−0.71	−0.57	–	0.69	−0.71	−0.61
SLA													
M1		1	–	0.62	–	–	0.40	–	0.53	–	−0.53	0.56	0.46
M2			1	–	–	–	–	–	–	−0.45	−0.50	–	–
SST													
M1				1	–	–	0.60	−0.43	0.72	–	−0.80	0.79	0.81
M2					1	–	–	–	–	–	–	–	–
S. Pacific													
CHL													
M1						1	–	−0.68	–	−0.54	0.46	−0.49	−0.42
SLA													
M1							1	–	0.54	–	−0.56	0.42	0.51
M2								1	0.38	0.40	−0.59	0.56	0.45
SST													
M1									1	–	−0.82	0.80	0.84
M2										1	–	–	–
Basin													
CHL													
M1											1	−0.95	−0.93
SLA													
M1												1	0.94
SST													
M1													1

both regions are negative anomalies during the 1997–1998 El Niño, strongest in the Humboldt Current. Thereafter, CHL variability is relatively weak in the Humboldt, stronger in the California region, where there are positive values in 2002, negative peaks in early 2004 and 2005, and a prolonged positive period over the last 5 years, maximum in 2008. In the California Current, values are strongest offshore of the Southern California Bight in the Ensenada frontal region where the main jet of the California Current turns eastward (Espinosa-Carreón et al., 2004; Thomas and Strub, 1990) and along the Oregon coast. Weakest patterns are in offshore regions off northern California and Baja California, and along the northern California coast (~38–40°N). In the Humboldt Current, patterns are strongest along the entire Peru coast and in a narrow coastal strip extending into northern Chile, consistent with the strong El Niño impacts (Carr et al., 2002; Thomas et al., 2001a) in these regions. Patterns are relatively strong off central Chile (~30–40°S), weakest in the offshore region off southern Peru–northern Chile and reversed at latitudes >~45°S where influences of Southern Ocean forcing become stronger (Montecino et al., 2006). CHL time series of the two regions are weakly correlated (Table 3) largely on the strength of the same strong El Niño signal in the first 12 months (Fig. 5). Weaker features in 2002, 2004 and 2005 appear out of phase. Correlations recalculated excluding the first 16 months (the strong ENSO), are not significant.

Comparisons of these CHL patterns to first modes of SLA and SST variability (Fig. 5(B) and (C)) show that large positive SLA and SST values are associated with the negative CHL signals during the El Niño period of 1997–1998 in both EBCs. SLA and SST in both EBCs are primarily negative for 1999–2002, the La Niña period, becoming positive in the period 2003–2006 in the California Current, while in the Humboldt Current time series are weak. All four SST and SLA time series are well correlated with each other (Table 3), indicating physical symmetry and suggesting common forcing. Their negative correlation with CHL variability, most strongly in the Humboldt Current, is consistent with

previous work showing strong coupling between the physical and biological processes in these region on interannual time scales (e.g., Carr et al., 2002; Chavez et al., 2002; Legaard and Thomas, 2006; Ulloa et al., 2001). One pattern that is consistently different between the two EBC regions in these three data sets is their latitudinal distribution (Fig. 5), weighted heavily towards the lowest latitudes in the Humboldt Current but relatively evenly weighted across the full latitudinal extent of the California Current. This difference reflects the lower latitudes included in the Humboldt Current, connecting the EBC wave guide directly to the El Niño signal. Substantial latitudinal propagation and travel around coastal features are required for this signal to arrive in the California system.

Alongshore wind stress (AWS, defined positive northward in both hemispheres) represents direct local forcing of coastal upwelling and enhanced summer CHL in the EBC regions. The dominant non-seasonal mode in each EBC region (Fig. 5(D)) has strong short-period temporal variability at highest latitudes, symptomatic of winter storm systems, resulting in a spatial mismatch between dominant non-seasonal wind forcing and the other satellite-measured variables (Fig. 5(A)–(C)). Correlations between the non-seasonal AWS and the ocean variables are weak or insignificant (Table 3). Of interest, however, are strong positive (negative) anomalies during El Niño in the California (Humboldt) Current revealing poleward (downwelling-favorable) AWS anomalies at latitudes >~35°N in the California Current and off central Chile (30–40°S). This supports an atmospheric connection and contribution to the negative CHL and positive SLA and SST anomalies at the higher latitudes. This pattern is reversed or absent in both systems at lower latitudes, reaffirming the role of poleward propagating SLA signals in creating the low latitude EBC anomalies.

How similar are dominant CHL patterns within the EBC regions to those over the whole basin? Spatially, California Current patterns (Fig. 5) are similar to those in this region calculated over the whole basin (Fig. 3) and their respective time series are correlated (Table 3). Dominant patterns in the Humboldt Current

Table 3

Correlations between modes 1 of non-seasonal variability within each EBC region of chlorophyll, SLA, SST and alongshore wind stress (Fig. 5) and to whole basin mode 1 (Fig. 3).

Region	California Current				Humboldt Current				Whole basin		
	CHL	SLA	SST	$\tau_{(as)}$	CHL	SLA	SST	$\tau_{(as)}$	CHL	SLA	SST
California Current											
CHL	1	−0.57	−0.67	−	0.43	−0.41	−0.57	−	0.46	−0.50	−0.41
SLA		1	0.87	−0.46	−0.55	0.77	0.62	−	−0.84	0.85	0.84
SST			1	−0.38	−0.46	0.65	0.58	−	−0.75	0.75	0.77
$\tau_{(as)}$				1	−	−	−	−	−	−	−
Humboldt Current											
CHL					1	−0.72	−0.70	−	0.52	−0.54	−0.53
SLA						1	0.83	−	−0.76	0.76	0.79
SST							1	−	−0.62	0.59	0.64
$\tau_{(as)}$								1	0.40	−0.43	−0.41
Basin											
CHL									1	−0.95	−0.93
SLA										1	0.94
SST											1

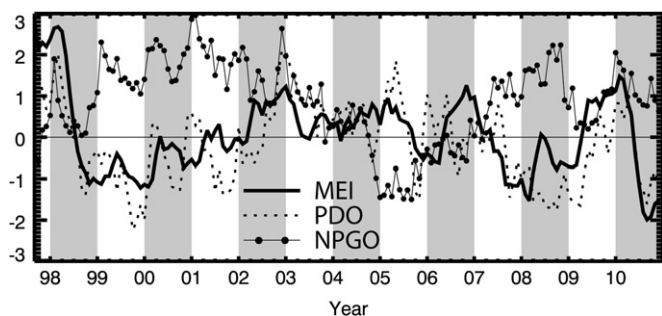


Fig. 6. Time series of three Pacific climate indices, the MEI, PDO and NPGO, over the study period.

have spatial similarities to both modes of basin-wide CHL variability (Fig. 3) and are temporally correlated with both ($r=0.52$ and 0.65 , respectively), each stronger than those in the California Current (emphasizing the Humboldt Current's more direct equatorial connection). Over the time window analyzed here, EBC CHL interannual variability is strongly related to that over the whole basin, contributing to the symmetry between systems and suggestive of common responses to climate signals of equatorial origin.

3.5. Satellite-measured variability: Relationships to climate indices

The strongest non-seasonal signal over the 13-year study period in most of the satellite-measured time series presented above is the 1997–1998 El Niño, associated with positive anomalies of SLA and SST and negative anomalies in CHL. The MEI (Fig. 6), designed to track ENSO equatorial variability (Wolter and Timlin, 1998), is strongly correlated with the dominant mode of non-seasonal variability of each satellite signal in each of the separate study areas (Table 4), most strongly (as expected) in the equatorial and whole basin regions for SST and SLA. ENSO impacts on equatorial SST, SLA and CHL patterns are well documented (McClain et al., 2002; Murtugudde et al., 1999), as are satellite views of CHL in the two EBC regions (Carr et al., 2002; Chavez et al., 2002; Kahru and Mitchell, 2000; Thomas et al., 2001a). The MEI tracks the dominant mode of merged CHL-SST non-seasonal variability over the whole Pacific (Martinez et al., 2009) and explains $\sim 21\%$ and 35% of mode 1 CHL variability in the California and Humboldt systems, respectively, over the complete SeaWiFS mission period. In the southern and northern

extra-tropics, the MEI accounts for 25% and 32%, respectively, of mode 1 CHL variance (Table 4), similar to its impact on the EBCs. The difference is that the ENSO has a stronger effect on the northern hemisphere extra-tropical band than on its EBC, while its direct connection to South America delivers a greater impact on the southern hemisphere EBC.

The first EOF of SST north of 20°N (Fig. 4) represents the purely satellite-data analog of the PDO (Fig. 6) over the 13-year study period. Not surprisingly, the space pattern looks indistinguishable from that of the PDO (see <http://jisao.washington.edu/pdo/>) and its time series is highly correlated (Table 4). The North Pacific EOFs of SLA and CHL (Fig. 4) are similar to that of SST, their time series are highly correlated (Table 2), and each is more strongly related to the PDO than the MEI (Table 4), the only region where this is true, reflecting their North Pacific emphasis. Chhak et al. (2009) discuss the linkage between SLA, SST and the PDO in the North Pacific. Satellite time series over both the whole basin and the equatorial region are correlated with the PDO, consistent with previous results (Martinez et al., 2009) and indicative of connections between equatorial dynamics (ENSO) and North Pacific physical variability discussed by many authors (Di Lorenzo et al., 2010; Newman et al., 2003; Strub and James, 2002c) but expanded here to include a biological component. Restricted to variability in the California Current, correlations to the PDO are strong for SLA and SST, present but weaker for chlorophyll. In the southern hemisphere, the PDO is correlated to SST over the extra-tropics but not the EBC (Table 4), similar to the strong correlation between the dominant modes of SST in the northern and southern extra-tropics (Table 2 and Fig. 4). Do these satellite data suggest a PDO-equivalent extra-tropical SST mode in the southern hemisphere? If so, does it resemble the PDO and is it connected to ENSO? Figs. 4 and 6 and Tables 2 and 4 provide affirmative answers. The dominant mode of satellite SST in the southern extra-tropics is similar (not identical) to its northern counterpart; their correlation represents a common 52% of their variance. Both are correlated with the MEI and PDO (Table 4) and basin-scale SST variability (Table 2), consistent with decadal-scale SST linkages into both extra-tropical hemispheres from ENSO forcing (Shakun and Shaman, 2009).

Defined as the second mode of SLA variability in the northeast Pacific, Di Lorenzo et al. (2008) suggest that the NPGO is the oceanic expression of the atmospheric forcing associated with the North Pacific Oscillation that in turn is connected to ENSO variability (Di Lorenzo et al., 2010). The NPGO represents low frequency gyre circulation variability with links to upwelling

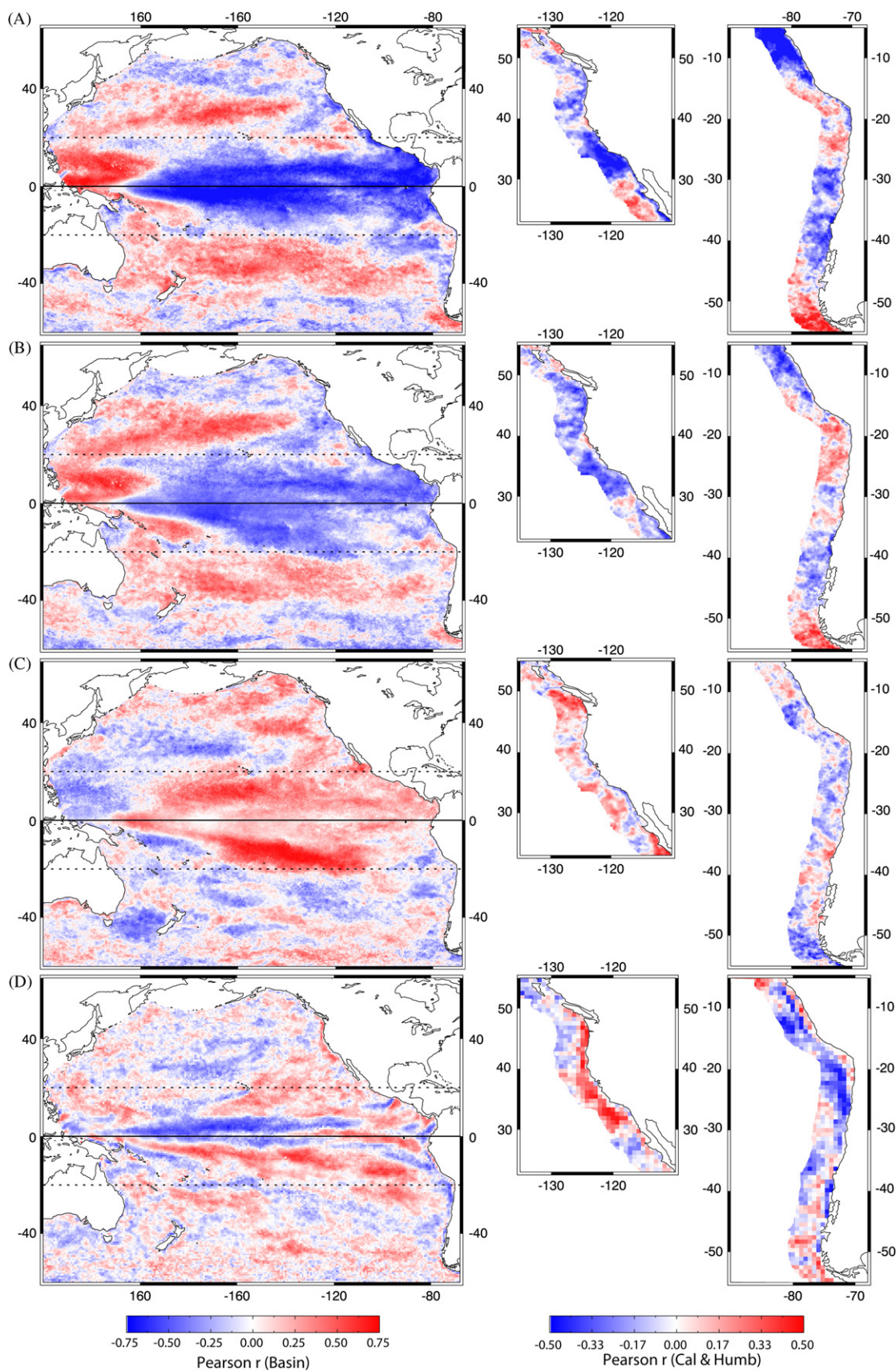


Fig. 7. Projection correlations that map the footprint of the (A) MEI, (B) PDO, (C) NPGO and (D) non-seasonal local wind stress curl (WSC) variability onto non-seasonal CHL at each grid location over the entire basin and in each EBC region. EBC values are the same as those over the basin but at higher spatial resolution and a different color scale to improve coastal details. The MEI, PDO and NPGO are a single time series correlated to CHL at each CHL grid location. In (D), CHL was re-mapped to the coarser resolution wind product grid and correlations of local wind stress curl with local CHL formed at each location.

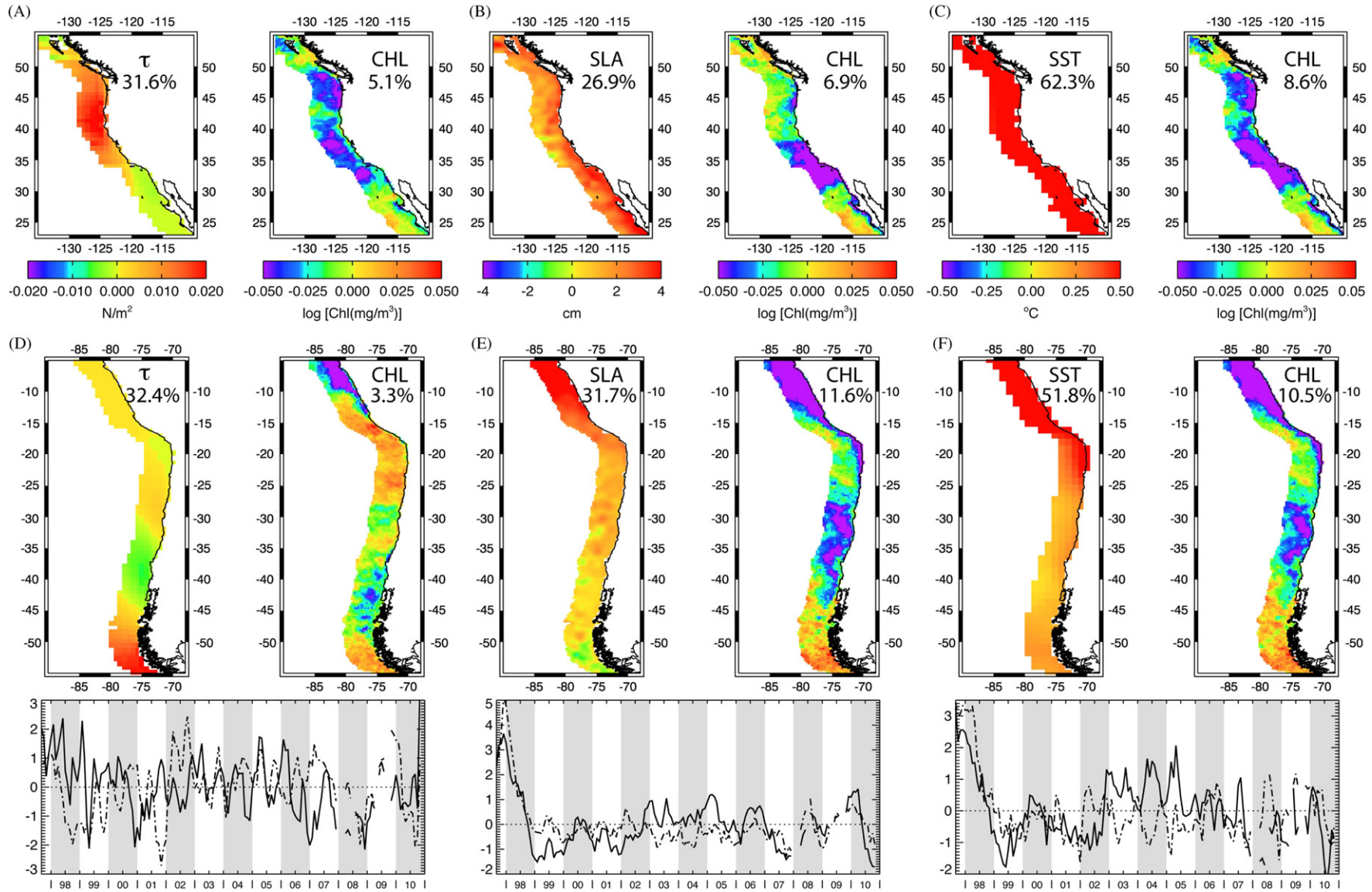


Fig. 8. Principal estimator patterns of CHL in the (A)–(C) California and (D)–(F) Humboldt EBC regions predicted by each of AWS (τ), SLA and SST, showing the pairs of predictor and estimand (CHL) space patterns, their common time series (solid line: California, dashed line: Humboldt), the percent of original predictor variance used by the PEP and the percent of the estimand (CHL) original total variance explained (“skill” of the PEP).

positive curl with increased CHL, but this is not true over the subtropical gyre and is strongly reversed in the equatorial corridor within 10° of the equator. This reversal at low latitudes is mirrored in the Southern Hemisphere where positive curl is associated with increased CHL anomalies. The implications are that in these low latitudes and the subtropical gyres, at the time and space scales addressed here, interannual variability in local WSC plays a weaker role in modulating CHL than other processes captured by the climate indices and satellite-measured SLA and SST and that these processes are associated with WSC signals opposite to those that cause upwelling.

3.6. Physical–biological coupling: Within EBC regions

PEPs quantify local EBC time and space coupling between dominant CHL modes of variability and physical modes, characterized here by AWS (τ), SLA and SST. In the California Current (Fig. 8(A)–(C)), differences in the spatial patterns of forcing and CHL responses can be interpreted in comparison to previously viewed time/space patterns. The AWS space pattern is strongest and positive at higher latitudes, decreasing sharply at $\sim 35^\circ\text{N}$, with weaker and reversed winds in the Southern California Bight and off Baja California, consistent with the geography of wind stress (Bakun and Nelson, 1991) that shows maxima off northern California and weaker, but more persistent upwelling winds off Baja California. The SLA pattern is weighted higher towards the coast and at lower latitudes, similar to SLA and SST in the Humboldt Current (Fig. 8(E) and (F)) and suggestive of coastally trapped signals arriving from low latitudes. California Current SST has no space pattern, implying a simple EBC-wide connection between high SST and low CHL. Poleward AWS and positive SST are coupled with similar negative CHL patterns; the main differences are extensions of lower CHL right to the California coast, throughout the Southern California Bight and continuous along Baja California coast in response to higher SST. CHL coupled to local SLA (Fig. 8(B)) is most similar to the CHL footprint of the MEI (Fig. 7), suggesting closer links to equatorial signals. Each California Current time series shows positive anomalies during the 1997–1998 El Niño period. Alongshore wind stress is positive northward, so association of positive time series with a positive wind spatial pattern indicates anomalously strong northward, or weaker equatorward (upwelling-favorable) winds during the El Niño. Thereafter, a number of events are recognizable from previous studies. Enhanced CHL concentrations linked to colder SSTs are evident in late 2001 and 2002, associated with an anomalous advection of colder, nutrient-rich subarctic waters into the northern California Current (Freeland et al., 2003; Thomas et al., 2003; Wheeler et al., 2003). In the first half of 2005, all three time series switch abruptly from strongly positive to weakly negative, the coupled response to delayed seasonal upwelling (Barth et al., 2007).

In the Humboldt Current (Fig. 8(D)–(F)), SLA and SST have similar spatial patterns strongly weighted to low latitudes. Each is dominated by positive 1997–1998 El Niño signals and each has considerably more “skill” driving non-seasonal CHL than AWS. Both are linked to similar CHL patterns, with maximum negative anomalies off Peru and coastal regions of northern Chile and again off central Chile $30\text{--}40^\circ\text{S}$. After the El Niño signal, the time series of both SLA and SST are weaker than those in the California Current. This, and the increased skill of SLA and SST PEPs in the Humboldt Current are likely due to more direct linkages to equatorial signals and relatively weaker local processes that influence non-seasonal CHL variability. The AWS pattern is dominated by variability at the highest latitudes where winds are dominated by Southern Ocean storms; non-seasonal AWS variability over lower latitudes is comparatively weak. CHL

variability, however, is strongest off Peru (Fig. 5(A)) and this mismatch likely explains the lower “skill” of this PEP.

3.7. Physical–biological coupling: Equatorial links to regional chlorophyll variability

EOFs and PEPs of variability at higher latitudes and in the EBC regions (Figs. 4, 5 and 8) are dominated by 1997–1998 El Niño signals, well correlated to the MEI (Table 4) and clearly linked to equatorial variability. Here we contrast the views of “local” coupling (Fig. 8) to those of non-local forcing of CHL by satellite-measured physical signals in the equatorial corridor. PEPs of equatorial SLA and SST generated substantially similar CHL patterns and time series, as expected from the strong correlation of dominant equatorial SLA and SST EOF modes (Table 1). For brevity we show only those of SLA forcing CHL.

PEPs of equatorial SLA (and SST, not shown) forcing EBC CHL are shown in Fig. 9(A) and (B). Equatorially forced California Current CHL PEP patterns are substantially similar to “local” coupling (Fig. 8) south of $\sim 38^\circ\text{N}$, but differ from those produced by local wind and SST (Fig. 8(A) and (C)) off Oregon and Washington. This suggests patterns at these higher latitudes have stronger links to local (or non-equatorial) wind forcing and associated SST response, consistent with links to NE Pacific atmospheric variability in this region (Barth et al., 2007; Freeland et al., 2003; Strub and James, 2002b). Their joint time series correlate with the MEI (0.75), but with a 1–2 month lag. In the Humboldt Current (Fig. 9(B)), equatorially forced CHL patterns are almost identical to those forced locally (Fig. 8(E) and (F)), and their joint time series correlation to the MEI is 0.75 with no lag, both consistent with a more direct connection to low latitude signals.

PEPs of equatorial SLA (and SST, not shown) forcing northern and southern hemisphere extra-tropical CHL variability (Fig. 9(C) and (D)) quantify coupling between equatorial signals (the satellite-derived analogs to the MEI) and biology at extra-tropical latitudes. These show biological patterns similar to those in Fig. 4: elevated equatorial SLA is associated with (a) increased CHL within the central gyres and (b) decreased CHL along the eastern rim of the basin, strongest off south-central California, into the Gulf of Alaska and off Chile. Equatorial SLA (and SST) patterns driving these CHL patterns, however, differ. Northern Hemisphere CHL is associated with forcing focused right along the equator, strongest in the central Pacific. The joint time series is synchronous with the MEI during 1997–1998 and lags it by ~ 2 months thereafter with an overall correlation of 0.81. Southern Hemisphere CHL is associated with equatorial SLA (and SST) patterns with a basin-wide zonal gradient, more similar to those evident in mode 2 of the basin-scale SLA EOF (Fig. 3) and suggestive of later, transitional stages of the ENSO cycle. The joint PEP time series is weakly (but significantly) correlated with the MEI (0.43) at a lag of 1 month. These differences point to more direct coupling of North Pacific CHL to equatorial signals with maximum coupling in each hemisphere linked to different phases of the ENSO cycle.

3.8. Summary and conclusions

Both seasonal and non-seasonal biological and physical variability in the Pacific measured by 13 years of concurrent satellite data (CHL, SLA and SST) have strong symmetry about the equatorial region. Seasonal patterns are strongest at mid latitudes and non-seasonal patterns are focused along the equatorial corridor.

Dominant modes of non-seasonal EOFs calculated over the whole basin and the equatorial ($0^\circ \pm 20^\circ$) region, are strongly correlated between regions and all variables, indicative of close biological–physical coupling and equatorial domination of Pacific

ENSO, the MEI is linked to the PDO and to the NPGO through the influence of atmospheric forcing on SST (and SLA) patterns at higher latitudes. Each also has connections to basin-scale wind stress curl patterns and alongshore wind stress in the EBC regions.

Overall, the two EBCs show a gradation from control of CHL at lower latitudes by SLA to control by winds at higher latitudes. In the California Current, PEPs show coupling between CHL and local wind, SLA and SST, weakest for wind at low latitudes; time series of SLA and SST indicate equatorial forcing. In the Humboldt Current, PEPs show wind has less interaction with chlorophyll interannual variability than SST and SLA, pointing to more direct connections of SLA and SST to equatorial signals. PEPs also show the direct interaction of equatorial SLA and SST variability on EBC and higher latitude CHL, confirming the above links in EBC regions. The PEPs show that northern hemisphere extra-tropical CHL lags equatorial signals by ~2 months and is most closely linked to El Niño anomalies in the central equatorial Pacific while southern hemisphere extra-tropical CHL response is weaker, not lagged, and more closely linked to transitional equatorial patterns of the ENSO cycle.

Lastly, these time series are short by climate standards; requiring merging with additional ocean color missions to address decadal changes (Antoine et al., 2005; Martinez et al., 2009), and too short to address anthropogenic influences on oceanographic variability (Henson et al., 2010). They do, however, demonstrate the extent to which a single consistent mission (a) can quantify and reveal patterns of large-scale variability related to climate and (b) reflect variability tracked by major climate indices. They provide spatial details in CHL coupling to SLA and SST patterns unavailable from in situ data. Lags between the MEI and PEP time series connecting equatorial SLA and California Current CHL spatial distributions highlight their potential predictive capabilities and emphasizes the need to continue these satellite observations into the future.

Acknowledgments

We thank the NASA SeaWiFS project team for providing the ocean color satellite data, AVISO, NOAA/NWS/NCEP and NCAR for access to SLA, SST and wind data products, respectively, and those people/organizations (referenced in the text) that make the various climate indices available. Funding for this work was provided by NSF as part of the U.S. GLOBEC program to ACT (OCE-0814413, OCE-0815051) and PTS (OCE-0815007). Additional support for PTS was provided by the NASA Ocean Surface Topography Science Team (NNX08AR40G). Three anonymous reviewers provided constructive comments that resulted in a longer but more complete manuscript. This is contribution 718 of the U.S. GLOBEC program.

References

Abbott, M.R., Barksdale, B., 1991. Phytoplankton pigment patterns and wind forcing off central California. *J. Geophys. Res.* 96, 14649–14667.

Anderson, P.J., Paitt, J.F., 1999. Community reorganization in the Gulf of Alaska following ocean climate regime shift. *Mar. Ecol. Prog. Ser.* 189, 117–123.

Antoine, D., Morel, A., Gordon, H.R., Banzon, V.F., Evans, E.H., 2005. Bridging ocean color observations of the 1980s and 2000s in search of long-term trends. *J. Geophys. Res.*, 110, <http://dx.doi.org/10.1029/2004JC002620>.

Bakun, A., Nelson, C.S., 1991. The seasonal cycle of wind-stress curl in subtropical eastern boundary current regions. *J. Phys. Oceanogr.* 21, 1815–1834.

Barth, J.A., Menge, B.A., Lubchenko, J., Chan, F., Bane, J.A., Kirincich, A.R., McManus, M.A., Nielsen, K.J., Pierce, S.D., Washburn, L., 2007. Delayed upwelling alters nearshore coastal ocean ecosystems in the northern California current. *Proc. Nat. Acad. Sci.* 104, 3719–3724.

Bond, N.A., Harrison, D.E., 2000. The Pacific Decadal Oscillation, air–sea interaction and central north Pacific winter atmospheric regimes. *Geophys. Res. Lett.* 27, 731–734.

Campbell, J.W., 1995. The lognormal distribution as a model for bio-optical variability in the sea. *J. Geophys. Res.* 100, 21327–21325.

Carr, M.E., Strub, P.T., Thomas, A.C., Blanco, J.L., 2002. Evolution of 1996–1999 La Nina and El Niño conditions off the western coast of South America: a remote sensing perspective. *J. Geophys. Res.*, 107, <http://dx.doi.org/10.1029/2001JC001183>.

Chavez, F.P., Messié, M., Pennington, J.T., 2011. Marine primary production in relation to climate variability and change. *Annu. Rev. Mar. Sci.* 3, 227–260, <http://dx.doi.org/10.1146/annurev.marine.010908.163917>.

Chavez, F.P., Pennington, J.T., Castro, C.G., Ryan, J.P., Michisaki, R.P., Schlining, B., Walz, P., Buck, K.R., McFadyen, A., Collins, C.A., 2002. Biological and chemical consequences of the 1997–1998 El Niño in central California waters. *Prog. Oceanogr.* 54, 205–232.

Chavez, F.P., Strutton, P.G., Friederich, C.E., Feely, R.A., Feldman, G.C., Foley, D.C., McPhaden, M.J., 1999. Biological and chemical response of the equatorial Pacific Ocean to the 1997–98 El Niño. *Science* 286, 2126–2131.

Chelton, D.B., Freilich, M.H., Esbensen, S.K., 2000. Satellite observations of the wind jets off the Pacific coast of central America. Part I: Case studies and statistical characteristics. *Monthly Weather Rev.* 128, 1993–2018.

Chhak, K., Di Lorenzo, E., 2007. Decadal variations in the California Current upwelling cells. *Geophys. Res. Lett.*, 34, <http://dx.doi.org/10.1029/2007GL032023>.

Chhak, K.C., Di Lorenzo, E., Schneider, N., Cummins, P.F., 2009. Forcing of low-frequency ocean variability in the northeast Pacific. *J. Clim.* 22, 1255–1276.

Christian, J.R., Murtugudde, R., Ballabrera-Poy, J., McClain, C.R., 2004. A ribbon of dark water: phytoplankton blooms in the meanders of the Pacific North Equatorial Countercurrent. *Deep Sea Res. II* 51, 209–228.

Cloern, J.E., Hieb, K.A., Jacobson, T., Sansó, B., Di Lorenzo, E., Stacey, M.T., Largier, J.L., Meiring, W., Peterson, W.T., Powell, T.M., Winder, M., Jassby, A.D., 2010. Biological communities in San Francisco Bay track large-scale climate forcing over the North Pacific. *Geophys. Res. Lett.*, 37, <http://dx.doi.org/10.1029/2010GL044774>.

Dandonneau, Y., Deschamps, P.-Y., Nicolas, J.-M., Loisel, H., Blanchot, J., Montel, Y., Thieuleux, F., Becu, G., 2004. Seasonal and interannual variability of ocean color and composition of phytoplankton communities in the North Atlantic, equatorial Pacific and South Pacific. *Deep Sea Res. II* 51, 303–318.

Davis, R.E., 1977. Techniques for statistical analysis and prediction of geophysical fluid systems. *Geophys. Astrophys. Fluid Dyn.* 8, 245–277.

Deser, C., Alexander, M.A., Xie, S.-P., Phillips, A.S., 2010. Sea surface temperature variability: patterns and mechanisms. *Annu. Rev. Mar. Sci.* 2, 115–143.

Di Lorenzo, E., Cobb, K.M., Furtado, J.C., Schneider, N., Anderson, B.T., Bracco, A., Alexander, M.A., Vimont, D.J., 2010. Central Pacific El Niño and decadal climate change in the North Pacific Ocean. *Nat. Geosci.* 3, <http://dx.doi.org/10.1038/NNGEO1984>.

Di Lorenzo, E., Schneider, N., Cobb, K.M., Chhak, K., Franks, P.J.S., Miller, A.J., McWilliams, J.C., Bograd, S.J., Arango, H., Curchister, E., Powell, T.M., Rivero, P., 2008. North Pacific Gyre Oscillation links ocean climate and ecosystem change. *Geophys. Res. Lett.*, 35, <http://dx.doi.org/10.1029/2007GL032838>.

Dommenget, D., Latif, M., 2002. A cautionary note on the interpretation of EOFs. *J. Clim.* 15, 216–225.

Echevin, V., Aumont, O., Ledesma, J., Flores, G., 2008. The seasonal cycle of surface chlorophyll in the Peruvian upwelling system: a modelling study. *Prog. Oceanogr.* 79, 167–176.

Espinosa-Carreón, T.L., Strub, P.T., Beier, E., Ocampo-Torres, F., Gaxiola-Castro, G., 2004. Seasonal and interannual variability of satellite-derived chlorophyll pigment, surface height, and temperature off Baja California. *J. Geophys. Res.* 109, <http://dx.doi.org/10.1029/2003JC002105>.

Freeland, H.J., Gatién, G., Huyer, A., Smith, R.L., 2003. Cold halocline in the northern California Current: an invasion of subarctic water. *Geophys. Res. Lett.* 30, <http://dx.doi.org/10.1029/2002GL016663>.

Halpern, D., 2002. Offshore Ekman transport and Ekman pumping off Peru during the 1997–1998 El Niño. *Geophys. Res. Lett.* 29, <http://dx.doi.org/10.1029/2001GL014097>.

Henson, S.A., Sarmiento, J.L., Dunne, J.P., Bopp, L., Doney, S.C., John, J., Beaulieu, C., 2010. Detection of anthropogenic climate change in satellite records of ocean chlorophyll and productivity. *Biogeosciences* 7, 621–640.

Hormazabal, S., Shaffer, G., Letelier, J., Ulloa, O., 2001. Local and remote forcing of sea surface temperature in the coastal upwelling system off Chile. *J. Geophys. Res.* 106, 16657–16671.

Kahru, M., Mitchell, B.G., 2000. Influence of the 1997–98 El Niño on the surface chlorophyll in the California Current. *Geophys. Res. Lett.* 27, 2937–2940.

Kahru, M., Mitchell, B.G., 2001. Seasonal and nonseasonal variability of satellite-derived chlorophyll and colored dissolved organic matter concentration in the California Current. *J. Geophys. Res.* 106, 2517–2529.

Kahru, M., Mitchell, B.G., 2002. Influence of the El Niño–La Niña cycle on satellite-derived primary production in the California Current. *Geophys. Res. Lett.* 29, <http://dx.doi.org/10.1029/2002GL014963>.

Large, W.G., Morzel, J., Crawford, G.B., 1995. Accounting for surface wave distortion of the marine wind profile in low-level ocean storms wind measurements. *J. Phys. Oceanogr.* 25, 2959–2971.

Legaard, K., Thomas, A.C., 2006. Spatial patterns in seasonal and interannual variability of chlorophyll and surface temperature in the California Current. *J. Geophys. Res.*, 111, <http://dx.doi.org/10.1029/2005JC003282>.

Lewis, M.R., Kuring, N., Yentsch, C., 1988. Global patterns of ocean transparency: implications for the new production of the open ocean. *J. Geophys. Res.* 93, 6847–6856.

Longhurst, A., 1995. Seasonal cycles of pelagic production and consumption. *Prog. Oceanogr.* 36, 77–167.

